

# Duplex-GS: Proxy-Guided Weighted Blending for Real-Time Order-Independent Gaussian Splatting

Weihang Liu, Yuke Li, Yuxuan Li, Jingyi Yu, *Fellow, IEEE*, Xin Lou, *Senior Member, IEEE*,

**Abstract**—Recent advances in 3D Gaussian Splatting (3DGS) have demonstrated remarkable rendering fidelity and efficiency. However, these methods still rely on computationally expensive sequential  $\alpha$ -blending operations, resulting in significant overhead—particularly on resource-constrained platforms. In this paper, we propose Duplex-GS, a dual-hierarchy framework that integrates proxy Gaussian representations with order-independent rendering techniques to achieve photorealistic results while sustaining real-time performance. To mitigate the overhead caused by view-adaptive radix sort, we introduce cell proxies for local Gaussians management and propose cell search rasterization for further acceleration. By seamlessly combining our framework with Order-Independent Transparency (OIT), we develop a physically inspired weighted sum rendering technique that simultaneously eliminates “popping” and “transparency” artifacts, yielding substantial improvements in both accuracy and efficiency. Extensive experiments on a variety of real-world datasets demonstrate the robustness of our method across diverse scenarios, including multi-scale training views and large-scale environments. Our results validate the advantages of the OIT rendering paradigm in Gaussian Splatting, achieving high-quality rendering with an impressive  $1.5\times-4\times$  speedup over existing OIT based Gaussian Splatting approaches and  $52.2\%-86.9\%$  reduction of the radix sort overhead without quality degradation.

**Index Terms**—Novel View Synthesis, Gaussian Splatting, Order-Independent Transparency, Real-Time Rendering

## I. INTRODUCTION

NOVEL view synthesis (NVS) and real-time rendering have attracted significant attention in both academia and industry, with broad applications in video games, virtual reality (VR) [1], and 3D scene reconstruction [2]–[5]. Inspired by the groundbreaking Neural Radiance Field (NeRF) [6], learning based methods have substantially advanced the realism of digital content, narrowing the gap between the virtual and real worlds. However, these methods often entail considerable computational overhead. The emergence of 3D Gaussian Splatting (3DGS) [7], [8] marks another milestone, enabling photorealistic and real-time rendering of radiance fields via rasterization—a paradigm akin to the graphics pipeline in modern graphics processing units (GPUs).

Despite the impressive reconstruction and rendering capabilities of 3DGS, a primary limitation is the need for an ever-increasing number of Gaussian primitives to fit all training views. This results in substantial and irregular memory access during rendering, as costly view-dependent sorting operations over long sequences impose considerable computational and memory overhead [9], [10]. Moreover, the sorting process

can introduce visible “popping” artifacts [11], as illustrated in Fig. 1. Collectively, these limitations hinder the scalability of 3DGS for large-scale applications and restrict its deployment on resource-constrained platforms such as mobile phones and VR devices.

More recently, sort-free Gaussian Splatting [12] has incorporated Order-Independent Transparency (OIT) [13], [14] into the Gaussian Splatting framework, eliminating the need for sorting in the rasterization pipeline by employing Weighted Sum Rendering (WSR) [15]. This effectively eliminates “popping” artifacts and has been successfully demonstrated on mobile devices [12]. However, as illustrated in Fig. 1, the absence of early termination when encountering opaque objects leads to “transparency” artifacts and increased rendering time, particularly in large-scale scenes, due to the accumulation of redundant Gaussian primitives in final blending.

Neural Gaussian framework [16], [17] is another line of work to enhance storage efficiency for 3DGS, which transitions from explicit 3D Gaussian primitives to a hybrid representation where clusters of Gaussians are encoded via “anchors” and associated with a shared MLP. However, this paradigm adheres to the conventional rendering pipeline and still operates on sets of 3D Gaussians decoded on-the-fly by the MLP. As a result, sorting the lengthy sequence of Gaussians remains mandatory for such Tile based Rendering (TBR), presenting substantial challenges for devices with limited resources [10]. Furthermore, since the spatial positions of neural Gaussians are not explicitly constrained by the anchor points, the generated Gaussians may deviate significantly from their associated anchors—as illustrated in Fig. 2—thereby complicating anchor management.

In this paper, we present Duplex-GS, which models 3D scenes with WSR rendering paradigm and dual-layered structure following the neural Gaussian framework. Firstly, scenes are encoded as explicit proxies that are easily stored and manipulated in the first layer. As the concept anchor degenerates the 3D Gaussian to point cloud, we introduce “cell” as the replacement, which is an ellipsoid with concrete physical geometry initialized at the Structure-from-Motion (SfM) [18] points. By constraining the emitted neural Gaussians located inside the cell region, the rasterization can be performed in cell level. Secondly, primitives are decoded as other forms, which is suitable for high-fidelity rendering in the second layer. Encouraged by [12], we introduce the physical inspired WSR with early termination where the specific order of Gaussian depth is not required, which replaces the non-commutative blending operations with parallelizable weighted sum operation. As the number of primitives in the first layer

This work has been submitted to the IEEE for possible publication. Copyright may be transferred without notice, after which this version may no longer be accessible.

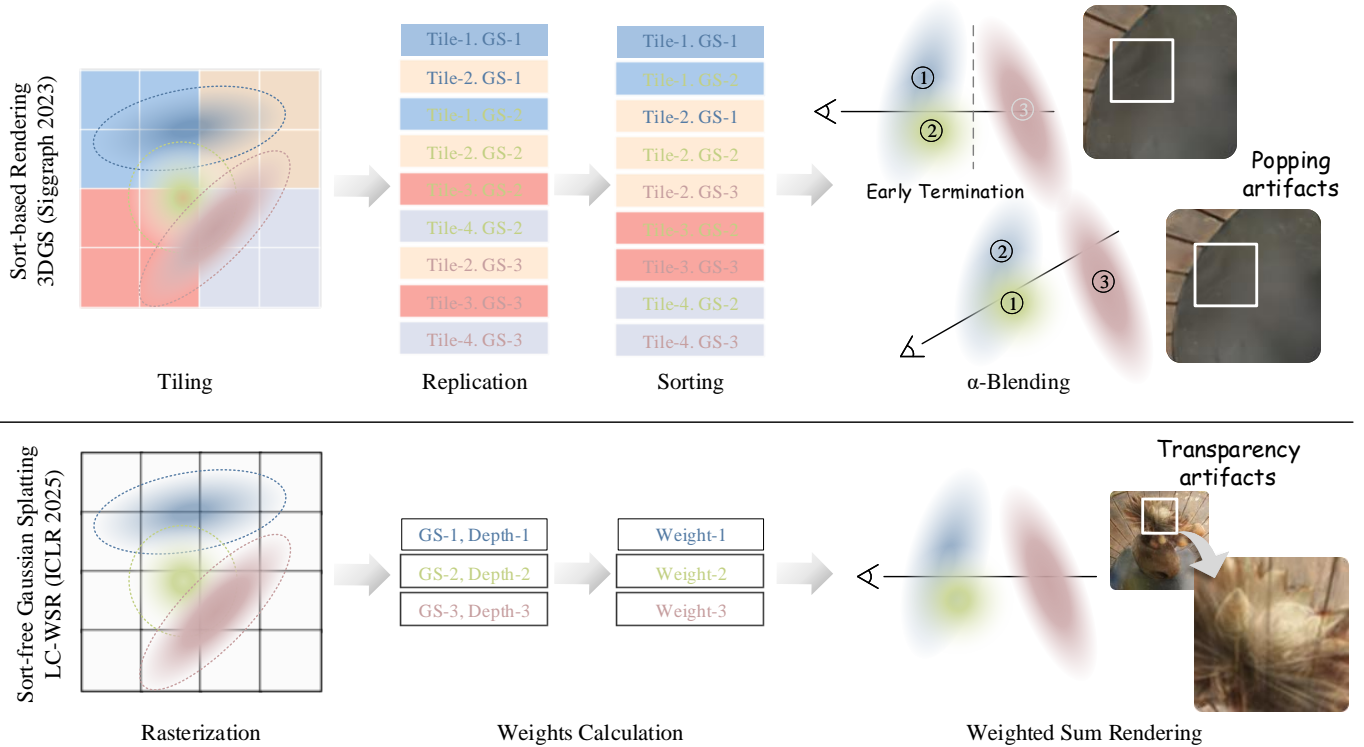


Fig. 1. **Motivation of Duplex-GS.** The rendering process for 3DGS rely on sorting for long tile-Gaussian sequence, introducing popping artifacts. The sort-free LC-WSR uses weighted sum rendering method without the need of consuming sorting stage, introducing transparency artifacts due to the lack of early termination when encounter opaque object.

is extensively fewer than that of Gaussians, the proposed cell search rasterization significantly reduce the memory and computational overhead introduced by radix sort. On the one hand, rasterization and lightweight sorting in the first layer removes the “transparency” artifact. On the other hand, the WSR kernel removes the “popping” artifact introduce by vanilla  $\alpha$ -blending.

In summary, the contributions of this work are as follow:

- We introduce a dual-layered Gaussian hierarchy, in which the first layer consists of proxies called cells and the second layer comprises 3D Gaussians. Our approach significantly alleviates the need for global sorting while preserving the parallelizability of WSR, thereby achieving artifact-free, real-time 3D reconstruction.
- **Cell rasterization in layer I:** We introduce cells—ellipsoids with adaptive geometric properties—to organize emitted Gaussians. Based on this structure, we propose a novel cell rasterization strategy that dramatically reduces both memory and computational overhead associated with radix sort.
- **Physical inspired WSR blending in layer II:** We retrieve physical constraints of Gaussian parameters for WSR method to blend Gaussians without the need for global sorting, inherently avoiding the “popping” artifact. Building on this, we introduce cell-level early termination to further accelerate rendering and effectively mitigate the “transparency” artifact encountered in the original WSR approach.
- We implement WSR based Gaussian Splatting on CUDA-

enabled platforms. Experimental results demonstrate that our method delivers comparable rendering speed and visual fidelity to existing approaches on commercial high-end GPUs.

## II. RELATED WORK

### A. Neural Representation for 3D Scene

Traditional scene reconstruction methods, such as SfM [18], [19] and Multi-View Stereo (MVS) [20], [21], often struggle to recover texture-less regions or handle challenging lighting variations. The advent of Neural Radiance Fields (NeRF) [6] has demonstrated the impressive capability of learning based models to achieve photorealistic reconstructions from sparse 2D images. Building on this, numerous efficient NeRF variants have been developed [22]–[24], making real-time rendering increasingly feasible on edge devices [25]. A significant breakthrough in the field is 3D Gaussian Splatting (3DGS) [7], which leverages explicit anisotropic 3D Gaussians for scene reconstruction and substantially accelerates rendering. Nevertheless, the substantial computational and memory demands of 3DGS continue to limit its applicability on resource-constrained platforms. Notably, a trend is witnessed that as scene representations become more explicit, rendering speed improves at the cost of increased memory requirements. And hybrid variants have emerged as a promising compromise between rendering efficiency and memory usage [16], [22], [26]. For instance, Instant-NGP [22] employs an explicit learnable hash table that maps 3D space to a multi-resolution

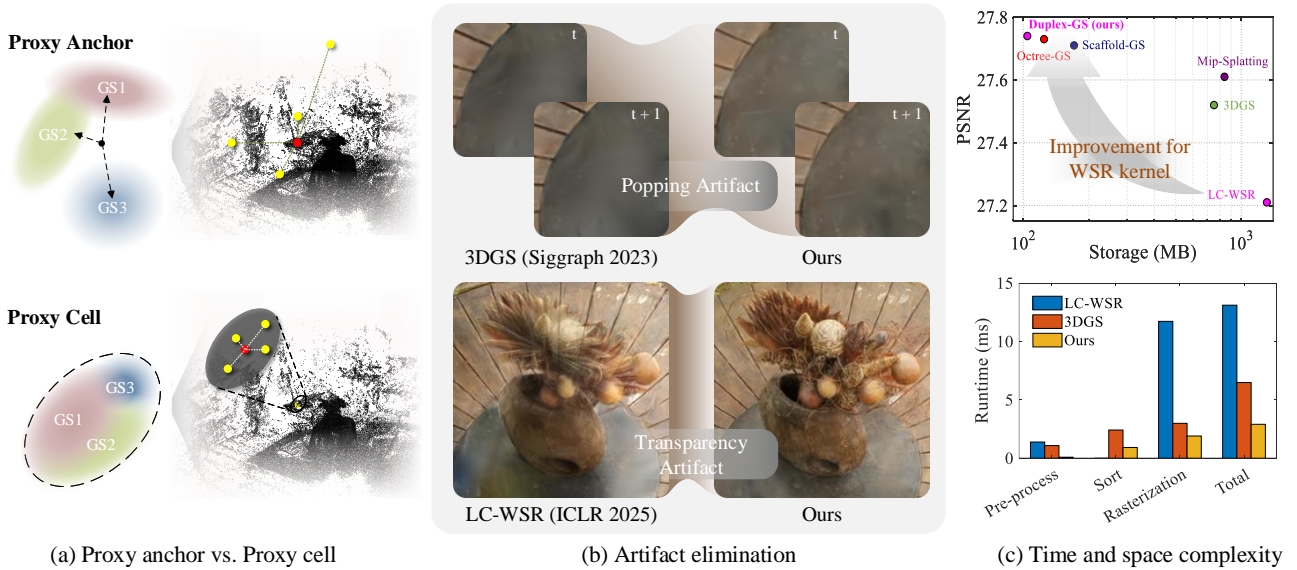


Fig. 2. **Overview of the proposed Duplex-GS.** The dual-hierarchy structure introduce cell as the proxy of local similar Gaussians. (a) Compared with proxy anchor, the proposed proxy cell is an ellipsoid with specific geometry. (b) Combing OIT rendering with 3DGS models, our method successfully remove the “popping” and “transparency” artifacts simultaneously. (c) By introducing cell search rasterization (Sec. IV) and physical weighted sum rendering (Sec. V), we achieve significant improvement over OIT Gaussian Splatting for both accuracy and efficiency.

grid, thereby alleviating the computational burden on the MLP. Scaffold-GS [16] introduces a hierarchical structure that encodes neural Gaussians using anchor points, achieving comparable rendering quality and speed with a significantly reduced model size. These advances enable fast, high-resolution rendering without compromising visual fidelity. However, these approaches still rely on the conventional blending pipeline requiring the Gaussians to be rendered in sorted depth order, typically achieved with tile based sorting algorithms. This sorting step not only complicates practical implementation but also introduces visual artifacts such as sudden changes in appearance, commonly referred to as “popping” artifacts [11].

### B. Efficient Neural Rendering

Unlike NeRF whose constraint is the high computational demand, the bottlenecks of 3DGS practical deployment are the extensive number of Gaussian primitives and the frequent memory access requirements [9], [10]. Various works aim to improve the efficiency of 3DGS by reducing the model size or the number of Gaussians involved in the sorting based blending operations [17], [27]–[29]. Encouraged by the OIT [13], [14], a widely deployed rendering paradigm in modern GPU to blend non-opaque media, sort-free Gaussian Splatting [12] introduce a novel blending paradigm WSR which eliminates the need of sorting operation in 3DGS, which removes the “popping” artifact as well as achieves faster rendering speed on mobile devices with small scale scenes. However, the lack of early termination results in the “transparency” artifacts as well as introduces extra computation when encounter opaque objects.

### C. Order Independent Transparency

Order-Independent Transparency (OIT) [13], [14] is a foundational graphics technique integrated into modern GPUs to enable the correct compositing of transparent fragments without requiring explicit depth sorting prior to rasterization. Early approaches, such as Depth Peeling [30], A-buffer [31], and Multi-Layer Alpha Blending (MLAB) [32], successfully achieve OIT but often incur significant time or memory overhead. Weighted Blended OIT [15] offers a more efficient alternative by approximating the integration of transparency in a single render pass, storing weighted sums of color and opacity with carefully designed blending weights. And this method has been applied to 3D Gaussian Splatting (3DGS) rendering [12]. However, the absence of early termination in [12] when encountering opaque regions can degrade both visual quality and rendering performance. In contrast, the proposed Duplex-GS framework integrates the core idea of early termination from depth peeling—halting compositing upon encountering fully opaque surfaces—with Weighted Blended OIT. As a result, Duplex-GS attains rendering quality and speed on par with state-of-the-art (SOTA) 3DGS models on high-end GPUs, while exhibiting strong potential for deployment on resource-constrained edge devices by alleviating the huge overhead of the view-adaptive sorting stage.

## III. PRELIMINARIES

### A. Gaussian Splatting

3D Gaussian Splatting [7] models scenes using anisotropic 3D Gaussian primitives and renders images through a rasterization based paradigm. Each 3D Gaussian  $G(\mathbf{x})$  is represented by a center coordinate  $\boldsymbol{\mu} \in \mathbb{R}^3$  and a covariance matrix  $\boldsymbol{\Sigma} \in \mathbb{R}^{3 \times 3}$ :

$$G(\mathbf{x}) = e^{-\frac{1}{2}(\mathbf{x}-\boldsymbol{\mu})^T \boldsymbol{\Sigma}^{-1}(\mathbf{x}-\boldsymbol{\mu})}, \quad (1)$$

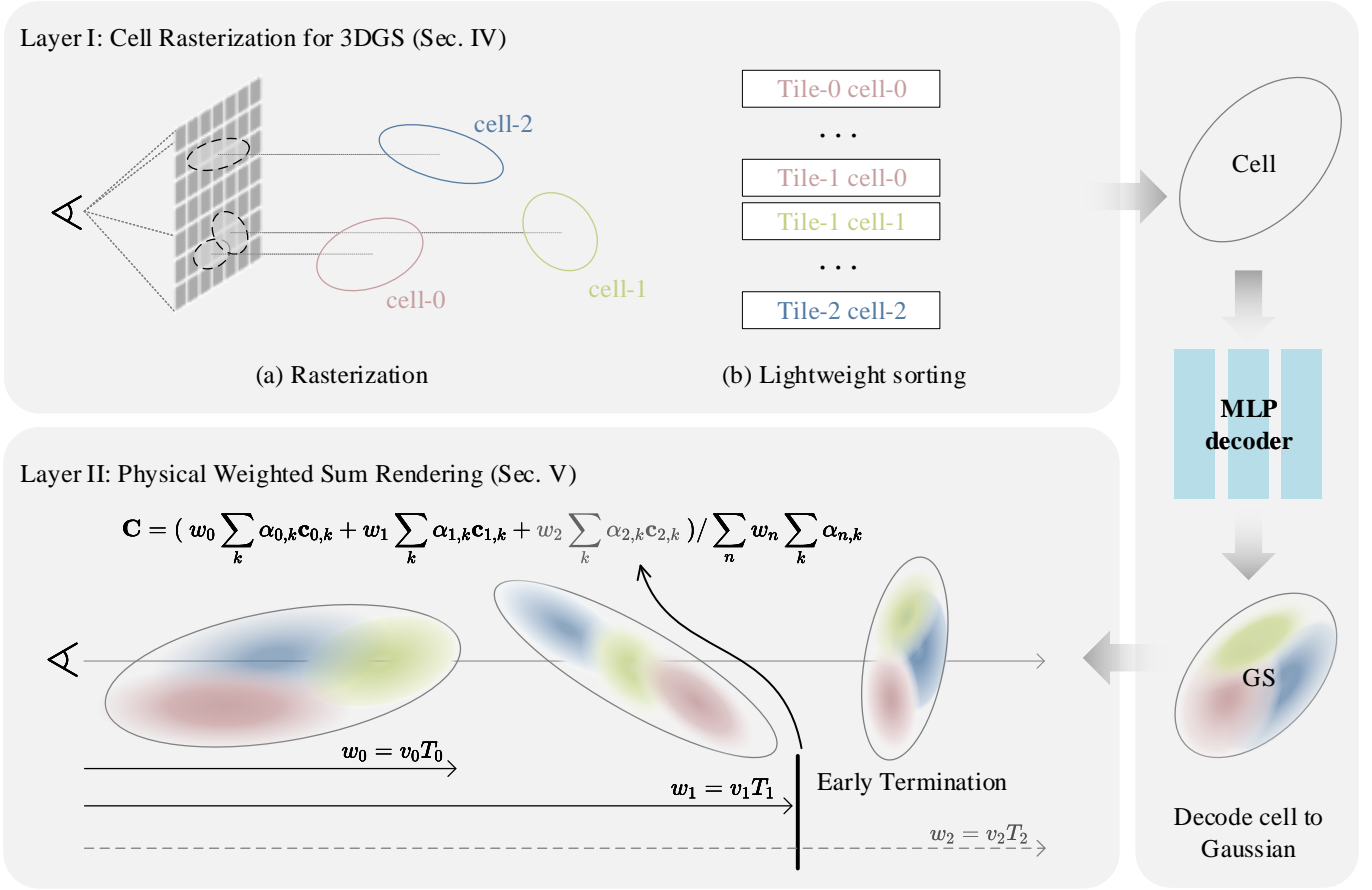


Fig. 3. **Illustration of the proposed Duplex-GS pipeline.** A dual-layered structure is designed to organize cells and Gaussians. In Layer I, proxy cells—represented as ellipsoids with specific geometric properties—are designed to aggregate Gaussians, enabling rasterization at the cell level and thereby alleviating the overhead associated with view-adaptive global sorting. Leveraging shared MLPs, the cell primitives are subsequently decoded into Gaussian primitives. In Layer II, the decoded Gaussians are blended using weighted sum rendering. Additionally, early termination technique is implemented—guided by the sorting results of the sparse cells from Layer I—which facilitates real-time, photorealistic rendering.

where  $\mathbf{x} \in \mathbb{R}^3$  is the queried position of the Gaussian kernel, and the covariance  $\Sigma$  is parameterized by scales  $\mathbf{s} \in \mathbb{R}^3$  and quaternions  $\mathbf{q} \in \mathbb{R}^4$ . In line with volumetric rendering conventions, each Gaussian is further associated with an opacity  $\sigma \in \mathbb{R}$  and a view-dependent color  $\mathbf{c} \in \mathbb{R}^3$ , which is commonly encoded using Spherical Harmonics (SH). Rendering proceeds via a tile based Gaussian rasterization technique, which employs efficient radix sort to enable  $\alpha$ -blending

$$\mathbf{C}(\mathbf{x}') = \sum_{i \in N} T_i^{\text{3DGS}} \mathbf{c}_i \alpha_i, \quad \alpha_i = \sigma_i G'_i(\mathbf{x}'), \quad (2)$$

where  $\mathbf{x}'$  denotes the 2D coordinates of the queried pixel,  $G'_i(\mathbf{x}')$  is the projected 2D gaussian kernel, and  $T_i^{\text{3DGS}}$  denotes the transmittance

$$T_i^{\text{3DGS}} = \prod_{j=1}^{i-1} (1 - \alpha_j). \quad (3)$$

### B. Scaffold-GS

Scaffold-GS introduces anchors as local encoding proxies, which emit neural Gaussians decoded from latent features to effectively represent local scene structure. Specifically, each

anchor emits a predefined set of  $K$  neural Gaussians, whose centers are given by:

$$\boldsymbol{\mu}_{n,k} = \mathbf{x}_n + \mathcal{O}_{n,k}^{\text{pos}} \cdot \mathbf{S}_n, \quad (4)$$

where  $n \in \{1, 2, \dots, N\}$  indexes the anchors,  $k \in \{1, 2, \dots, K\}$  indexes the neural Gaussians per anchor,  $\mathbf{x}_n$  denotes the center of anchor- $n$ , and  $\boldsymbol{\mu}_{n,k}$  represents the center of the emitted neural Gaussian- $k$ .  $\mathcal{O}_{n,k}^{\text{pos}}$  is the learned offset scaled by  $\mathbf{S}_n$ . Additionally, the opacities of the  $K$  neural Gaussians are decoded from the latent feature  $\mathbf{f}_n$ , viewing distance  $\delta_n$  and direction  $\mathbf{r}_n$  via a scene-wise MLP

$$\{\sigma_{n,1}, \dots, \sigma_{n,K}\} = F_\sigma(\mathbf{f}_n, \delta_n, \mathbf{r}_n), \quad (5)$$

where  $F_\sigma$  is the shared opacity decoder. Similarly, the other attributes of each neural Gaussians, including color  $\mathbf{c}_{n,k}$ , scales  $\mathbf{s}_{n,k}$  and quaternions  $\mathbf{q}_{n,k}$ , are predicted by the separate MLPs  $F_c$ ,  $F_s$ ,  $F_q$ , respectively.

### C. Weighted Sum Rendering

Inspired by Order Independent Transparency (OIT)—a widely adopted technique for rendering transparent media in traditional graphics pipelines—sort-free Gaussian Splatting

integrates this concept into 3DGS, producing the final image as

$$\mathbf{C} = \frac{\mathbf{c}_B w_B + \sum_{i=1}^N \mathbf{c}_i \alpha_i w(d_i)}{w_b + \sum_{i=1}^N \alpha_i w(d_i)}, \quad (6)$$

where  $\mathbf{c}_B$  and  $w_B$  denote the background color and the learnable background weights respectively, and  $d_i$  indicates the depths of the  $i$ -th 3D Gaussians.

By employing this WSR formulation, the non-commutative, computationally intensive sorting stage—traditionally required for compositing—is eliminated. This significantly enhances the potential for parallelization and accelerates rendering. Specifically, the SOTA Linear Correction weighted-sum rendering (LC-WSR) function  $w(d_i)$  is defined as

$$w(d_i) = T_i^{\text{LC-WSR}} \cdot v_i, \quad (7)$$

$$T_i^{\text{LC-WSR}} = \max\left(0, 1 - \frac{d_i}{\tau}\right), \quad (8)$$

where  $\tau$  and  $v_i$  are the learnable parameters. This function formulates the decay trend w.r.t. the depths of the rendering Gaussians.

#### IV. LAYER I: CELL RASTERIZATION FOR 3DGS

While neural Gaussian frameworks [16], [17] have achieved remarkable reconstruction accuracy, the use of anchors as encoding proxies lacks a concrete geometric interpretation. So we redesign the neural Gaussian proxies to alleviate the computational overhead associated with sorting and rasterization. Specifically, instead of encoding 3D Gaussians with anchors, we introduce the concept of “cell”—an ellipsoid with explicit geometric properties and a defined visible region—to encode neural Gaussians together with their latent features. Based on this representation, we further propose a cell rasterization strategy, enabling efficient and lightweight rasterization.

##### A. Cell Proxy

Unlike anchors, which are points lacking geometric structure, each cell is represented as an ellipsoid that contains several neural 3D Gaussians whose physical properties are dynamically decoded from a trainable feature.

Initialization begins with SfM points  $\mathbf{P} \in \mathbb{R}^{N \times 3}$ , from which we generate the initial cells, each centered at a point in accordance with the method described in [17]. Every cell is parameterized by physical structure scales  $\mathbf{S}_n$  and quaternions  $\mathbf{Q}_n$ , defining its visible region. In the dual-layered hierarchy, each cell is further associated with a latent feature vector  $\mathbf{f}_n$  that encodes local scene information, and emits  $K$  neural Gaussians as described in Eq. 4. The attributes of these  $K$  neural Gaussians—including color  $\mathbf{c}_{n,k}$ , scales  $\mathbf{s}_{n,k}$  and quaternions  $\mathbf{q}_{n,k}$ —are decoded from the latent feature  $\mathbf{f}_n$ , along with the viewing distance  $\delta_n$  and viewing direction  $\mathbf{d}_n$ , via shared scene-wise MLPs.

To ensure that each Gaussian center lies within the visible region of its corresponding cell, we constrain the offset parameter  $\mathcal{O}_{n,k}^{\text{pos}}$  to the range  $[-1, 1]$ . Additionally, to align the collective regions of the emitted neural Gaussians with the visible extent of the cell, we modify the encoding of the scale

$\mathbf{s}_{n,k}$  and quaternions  $\mathbf{q}_{n,k}$  attributes, thereby directly linking the geometric properties of the cell and its Gaussians

$$\{\mathcal{O}_{n,1}^{\text{scale}}, \dots, \mathcal{O}_{n,K}^{\text{scale}}\} = F_s(\mathbf{f}_n, \delta_n, \mathbf{d}_n), \quad (9)$$

$$\{\mathbf{q}_{n,1}, \dots, \mathbf{q}_{n,K}\} = F_q(\mathbf{f}_n, \delta_n, \mathbf{d}_n), \quad (10)$$

where the output of  $F_s$  and  $F_q$  are activated by sigmoid and normalization respectively. Furthermore, the overall geometric configuration of each cell is explicitly associated with that of its constituent Gaussians through

$$\mathbf{s}_{n,k} = \mathcal{O}_{n,k}^{\text{scale}} * \mathbf{S}_n, \quad (11)$$

$$\mathbf{Q}_n = \text{norm}\left(\sum_k \mathbf{q}_{n,k} * \sigma_{n,k}\right), \quad (12)$$

To restrict that the Gaussian regions fully locate inside the cell region, the maximum of  $\mathcal{O}_{n,k}^{\text{scale}}$  is clamped by

$$\mathcal{O}_{n,k}^{\text{scale}} = \min\left(\mathcal{O}_{n,k}^{\text{scale}}, 1 - \|\mathcal{O}_{n,k}^{\text{pos}}\|\right). \quad (13)$$

As illustrated in Fig. 3, the proposed neural Gaussians are constrained to reside strictly within their corresponding cell regions. Leveraging this property, the cell projections can effectively guide the Gaussian blending process.

##### B. Cell Searching Rasterization

In the original 3DGS framework [7], views are rendered by rasterizing 3D Gaussians onto the image plane through a Gaussian search rasterization strategy. In contrast, the anchors introduced in [16], which form the proxies of the dual-layered hierarchy, do not directly participate in the rendering process; instead, rendering remains confined strictly to the Gaussian level. This results in a distribution mismatch between the two hierarchy levels, i.e., between anchors and 3D Gaussians.

Building on our proposed geometric cell, we introduce a cell search rasterization technique in which cells, rather than individual Gaussians, serve as the primary rasterization units. As illustrated in Fig. 3, we perform rasterization at the cell level during the pre-processing stage, which reduces memory access overhead. Specifically, each cell defines a visible region, and only those whose regions intersect with the viewing frustum are recorded and subsequently decoded into neural 3D Gaussians for the subsequent  $\alpha$ -blending stage. This strategy ensures that the distribution of cells and 3D Gaussians are naturally aligned across the two hierarchy levels, and restricts rasterization exclusively to the cell level. Following the tile based paradigm, cells are assigned to individual tiles, and radix sort is applied to the cell sequence as necessary. Because each cell encapsulates a local cluster of Gaussians, the total number of cells is substantially less than the number of individual Gaussians. As a result, both memory consumption and computational overhead during rasterization are significantly reduced.

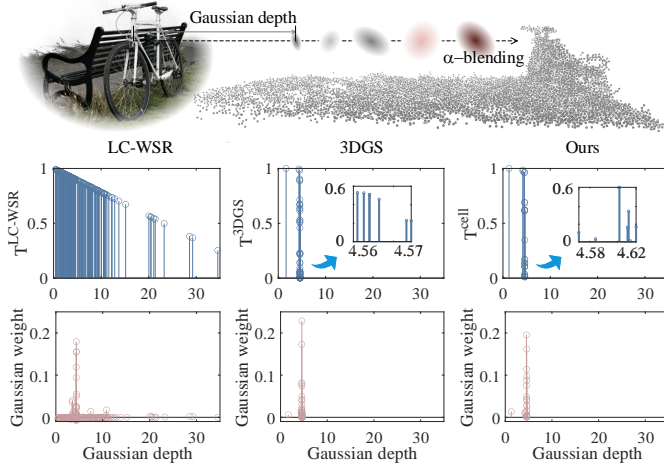


Fig. 4. Comparison of three different transmittance: LC-WSR (Eq. 8), vanilla 3DGS (Eq. 3) and ours (Eq. 16). The proposed transmittance is not strictly monotonically decreasing with increasing depth, indicating that the Gaussians are locally unordered. Nevertheless, our method achieves blending weights similar to those of vanilla 3DGS, without requiring an explicit Gaussian order.

## V. LAYER II: PHYSICAL WEIGHTED SUM RENDERING

Duplex-GS reconstructs 3D scenes using ellipsoidal cells, enabling rasterization and sorting to be performed at the cell level, thereby significantly reducing rasterization overhead. However, without explicitly sorting the depths of individual Gaussians—a requirement in the original  $\alpha$ -blending operations grounded in physical modeling—the exact blending order becomes ambiguous. Sort-free Gaussians [12], an OIT extension of vanilla 3DGS, demonstrated that optimized components and parameters for high-fidelity view synthesis are governed solely by the mathematical constraints of the scene model. This weighted sum approach is well-suited for integrating 3DGS into modern GPU graphics pipelines and for deployment on resource-constrained devices. Nevertheless, abandoning physical constraints introduces “transparency” artifacts that degrade visual quality, and the absence of early termination further results in reduced rendering efficiency.

In this section, we integrate the OIT based rendering paradigm with a cell based Gaussian model, retrieving physical constraints for WSR based 3DGS.

### A. Physical OIT Blending for 3DGS

WSR [12] is a mathematically motivated rendering model, in which  $\alpha_i$  in Eq. 6 does not directly represent the meaningful opacity of a Gaussian and may even exceed one due to its lack of a physical basis. While this formulation facilitates the weighted sum rendering process, it inherently precludes the early-termination mechanisms used in conventional  $\alpha$ -blending.

Obtaining the sorted order at the cell level is both memory and computationally efficient, since the number of cells is substantially fewer than that of the 3D Gaussians. Leveraging this, we redefine  $\alpha$  as the opacity weighted by the Gaussian kernel, as specified in Eq. 2, constraining its value to the physically meaningful range of  $[0, 1]$ .

Thanks to the approximate ordering provided by cell-level sorting—which adequately reflects the relative relationships among the contained Gaussians—we are able to enforce physical constraints within the mathematical WSR framework, without the need for precise ordering of all Gaussians. As illustrated in Fig. 3, the final rendered view  $C$  is computed according to the weighted sum rendering formula:

$$C = \frac{\sum_{n=1}^N w_n \sum_{k=1}^K \alpha_{n,k} c_{n,k}}{\sum_{n=1}^N w_n \sum_{k=1}^K \alpha_{n,k}}, \quad (14)$$

where  $w_n$  denotes the weight of cell- $n$ , derived from the cell-level sorting results. A sophisticated WSR kernel for each cell,  $w_n$  can then be defined as:

$$w_n = v_n \cdot T_n^{\text{cell}}, \quad (15)$$

where  $T_n^{\text{cell}}$  denotes the cell-level transmittance, which is efficiently obtained by sorting the sparsely distributed cells and can be calculated as:

$$T_n^{\text{cell}} = \prod_{i=1}^{n-1} \prod_{k=1}^K (1 - v_i \cdot \alpha_{i,k}). \quad (16)$$

Due to the non-uniform distribution and potential overlap of cells,  $T_i^{\text{3DGS}}$  in Eq. 3 may not precisely capture the transmittance of all emitted neural Gaussians. The introduction of the learnable parameter  $v_n$  for each cell effectively compensates for this approximation. Three relevant paradigms of transmittance and the resulting Gaussians weights are visualized in Fig. 4. LC-WSR simulates the decay trend of transmittance with a linear function w.r.t. Gaussian depth, introducing great number of Gaussians with tiny weights. Our method obtain similar weights compared with the vanilla 3DGS without the requirements of concrete order of individual Gaussians.

### B. Early Termination for Cell Based 3DGS

We propose to perform sorting based on cells, rather than individual Gaussians, thereby significantly reducing sorting overhead while retaining the hardware-friendly weighted sum rendering paradigm.

As  $T_n^{\text{cell}}$  decreases during the front-to-back rendering of cells, early termination can be efficiently incorporated to accelerate the rendering process and mitigate transparency artifacts. Specifically,  $T_n^{\text{cell}}$ , defined in Eq. 16, approaches zero as cell-level transmittance accumulates and saturates, which provides a practical criterion for early termination: the blending process is halted when  $T_n^{\text{cell}} < \epsilon$ . Furthermore, in contrast to previous WSR methods for 3DGS, our approach restores explicit physical meaning to the opacity parameter  $\sigma_{n,k}$ , restricting it to the range  $[0, 1]$ . This property facilitates pruning and regularization during training.

## VI. OPTIMIZATION STRATEGIES FOR CELL BASED GAUSSIAN SPLATTING

The proposed cell primitives are endowed with distinct physical attributes; however, these features are not directly involved in the differentiable blending process. Furthermore, advanced optimization strategies are introduced to systematically organize the evolving cell structures.

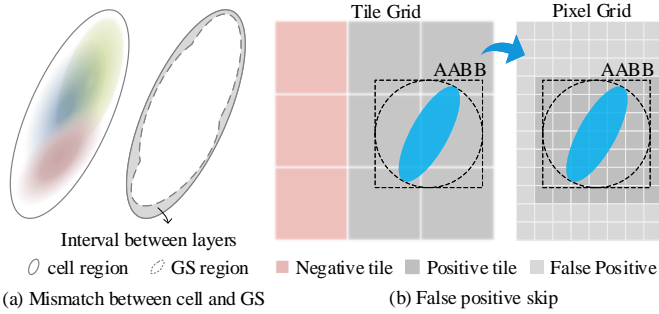


Fig. 5. Illustration of mismatch between cell and Gaussian. (a) The interval between layers influence the efficiency of cell rasterization. (b) False positive regions are skipped to alleviate the speed degradation from the mismatch.

### A. Alignment of Cell and Gaussian Region

The cell search rasterization inevitably leads to the introduction of redundant 3D Gaussians during the blending stage, due to the discrepancies that arise between the spatial intervals of cells and the emitted neural Gaussians. Furthermore, the efficiency of cell search rasterization is contingent upon the degree of coherence between the visible regions of a cell and its associated Gaussians.

1) *False positive skip*: TBR is widely adopted in modern GPUs and is also utilized in 3DGS rasterization. However, this approach often introduces a substantial number of redundant false-positive Gaussians, a problem that is further exacerbated in cell based Gaussian frameworks due to the spatial mismatch between cell regions and the actual coverage of Gaussians. To mitigate the associated performance degradation, we introduce a pixel-level radius based culling strategy to eliminate unnecessary Gaussian kernel computations. Specifically, as illustrated in Fig. 5, a lightweight axis-aligned bounding box (AABB) check is employed: Gaussians are excluded from the blending operation if the pixel lies outside their respective AABBs. This efficient early-exit mechanism significantly reduces redundant computation and accelerates the overall rendering process.

2) *Geometric correction via neural Gaussians*: In addition to skipping false-positive Gaussians to improve efficiency, maximizing the overlap between each cell and its emitted neural Gaussians further reduces the number of redundant Gaussians. To achieve better geometric alignment, we dynamically define the cell’s quaternion as a weighted average of the quaternions associated with its emitted Gaussians, as described in Eq. 12. Moreover, to ensure an even spatial distribution of Gaussians within each cell, the cell centers are periodically updated according to

$$\mathbf{x}_n = \frac{\sum_{k=1}^K \mu_{n,k}}{K}. \quad (17)$$

As cell scales are differentiable via Eq. 11, the three-dimensional covariances and positions of first-layer cells are learned in accordance with the updates to the second-layer Gaussians.

3) *Cell position reset*: As discussed in Gaussian based models [7], [16], [17], the initial SfM point cloud often fails to comprehensively cover the entire scene, particularly

in textureless or sparsely observed regions. Following the adaptive density control (ADC) policies employed in previous works [7], we utilize view-space positional gradients as a densification score to guide the growth of new cells. Specifically, additional cells are introduced at the centers of Gaussians that attain high densification scores. In contrast to the anchors proposed in [16], [17], which do not participate directly in the rendering process, our cells possess explicit physical attributes and independently encode local regions. To decouple existing cells from newly introduced ones, the offsets of the significant Gaussians are reset to zero after cell growth, i.e., their positions are reinitialized to the centers of the corresponding cells.

### B. Perceptual Loss

The loss function for optimizing 3D Gaussian Splatting (3DGS) is typically formulated as a combination of  $\ell_1$  and SSIM [33] losses, which respectively capture pixel-level reconstruction error and structural similarity. Minimizing these terms promotes high signal-to-noise ratios but often results in images that lack high-frequency details and appear perceptually unsatisfying, particularly at higher resolutions. Given the effectiveness of perceptual loss functions in image generative models [34], [35], we additionally incorporate a perceptual loss term for training Gaussian based models. The overall loss is defined as

$$\mathcal{L} = (1 - \lambda_1 - \lambda_2)\mathcal{L}_1 + \lambda_1\mathcal{L}_{\text{SSIM}} + \lambda_2\mathcal{L}_{\text{LPIPS}}, \quad (18)$$

where  $\mathcal{L}_1$ ,  $\mathcal{L}_{\text{SSIM}}$  and  $\mathcal{L}_{\text{LPIPS}}$  denote  $\ell_1$ , structural similarity and perceptual loss respectively. While the inclusion of the perceptual loss yields rendering results with improved perceptual quality, its computation relies on convolutional neural networks (CNNs), which increases the training time. To address this, we compute the perceptual loss every 20 training iterations, which substantially alleviates the additional computational overhead without noticeably increasing the overall training time.

## VII. EXPERIMENTAL RESULTS

### A. Experimental Settings

1) *Datasets*: We conducted extensive experiments on 31 realistic scenes drawn from various datasets, following the configurations in 3DGS [7] and Scafold-GS [16]. Specifically, we evaluated 13 publicly released datasets, including nine from Mip-NeRF360 [36], two from Tanks and Temples [37] and two from DeepBlending [38]. Additionally, we tested 10 further scenes—eight from BungeeNeRF [40] and two from VR-NeRF [1]—to assess the robustness of our approach in relatively large-scale environments. Scenes from BungeeNeRF feature multi-scale outdoor city scenes for validating view-adaptive rendering, while those from VR-NeRF provide intricate indoor scenes to evaluate detailed rendering capabilities.

2) *Metrics*: We evaluate the reconstruction fidelity with PSNR, SSIM [33] and LPIPS [41], which are commonly used in image quality measurement. We also record the model size, frame per second (FPS) as indicators of storage overhead and rendering speed. Additionally, the consumptions of the radix

TABLE I  
 QUANTITATIVE COMPARISONS ON REAL-WORLD DATASET [36]–[38]. DUPLEX-GS ACHIEVES COMPETITIVE RENDERING QUALITY WHILE REDUCING MODEL SIZE COMPARED TO THE BASELINES. THE BEST PERFORMANCE FOR EACH METRIC IS HIGHLIGHTED.

Method	Mip-NeRF360				Tanks & Temples				Deep Blending			
	PSNR $\uparrow$	SSIM $\uparrow$	LPIPS $\downarrow$	Storage $\downarrow$	PSNR $\uparrow$	SSIM $\uparrow$	LPIPS $\downarrow$	Storage $\downarrow$	PSNR $\uparrow$	SSIM $\uparrow$	LPIPS $\downarrow$	Storage $\downarrow$
Mip-NeRF360 <sup>1</sup> [36]	27.69	0.792	0.237	-	22.22	0.759	0.257	-	29.40	0.901	0.245	-
3DGS <sup>1</sup> [7]	27.52	0.813	0.222	750.2 MB	23.57	0.845	0.180	431.4 MB	29.61	0.900	0.251	662.7 MB
Mip-Splatting <sup>1</sup> [39]	27.61	<b>0.816</b>	<b>0.215</b>	838.4 MB	23.96	0.856	0.171	500.4 MB	29.56	0.901	0.243	736.8 MB
Scaffold-GS <sup>1</sup> ( $K = 10$ ) [16]	27.73	0.812	0.226	171.0 MB	24.09	0.858	0.165	147.7 MB	30.42	<b>0.912</b>	0.246	111.2 MB
Scaffold-GS <sup>1</sup> ( $K = 5$ ) [16]	27.74	0.811	0.230	205.3 MB	24.53	0.863	0.162	177.7 MB	30.26	0.911	0.242	143.4 MB
Octree-GS <sup>1</sup> ( $K = 10$ ) [17]	27.88	<b>0.816</b>	0.216	142.7 MB	<b>24.60</b>	0.864	0.157	77.8 MB	<b>30.44</b>	0.911	0.239	95.5 MB
Octree-GS <sup>1</sup> ( $K = 5$ ) [17]	27.73	0.813	0.227	124.5 MB	24.47	0.861	0.168	<b>73.9 MB</b>	30.06	0.908	0.250	<b>75.1 MB</b>
LC-WSR <sup>2</sup> [12]	27.21	0.800	0.219	1312.0 MB	23.22	0.832	0.186	672.7 MB	29.90	0.901	0.243	810.7 MB
Ours ( $K = 10$ )	<b>27.90</b>	0.813	0.216	152.2 MB	24.26	<b>0.867</b>	0.150	124.8 MB	30.30	0.910	0.249	89.7 MB
Ours ( $K = 5$ )	27.74	0.802	0.218	<b>104.4 MB</b>	24.32	<b>0.867</b>	<b>0.138</b>	112.2 MB	30.26	0.909	<b>0.236</b>	94.7 MB

<sup>1</sup> Experiments are conducted using the official public repository, with no modifications except for iteration settings as described in Sec. VII-A4.

<sup>2</sup> The official implementation has not been released. Experiments are conducted using our own implementation, which is available at <https://github.com/LiYukeee/sort-free-gs>.

TABLE II  
 QUANTITATIVE COMPARISONS ON BUNGEE NeRF [40] AND VR-NeRF [1] DATASETS. ADDITIONAL EXPERIMENTS ASSESS PERFORMANCE ON MULTI-SCALE RENDERING AND THE RECONSTRUCTION OF INTRICATE INDOOR DETAILS. DUPLEX-GS ACHIEVES HIGH-QUALITY RENDERING WITH COMPACT MODEL SIZES. THE BEST RESULT FOR EACH METRIC IS HIGHLIGHTED.

Method	BungeeNeRF				VR-NeRF: apartment				VR-NeRF: kitchen			
	PSNR $\uparrow$	SSIM $\uparrow$	LPIPS $\downarrow$	Storage $\downarrow$	PSNR $\uparrow$	SSIM $\uparrow$	LPIPS $\downarrow$	Storage $\downarrow$	PSNR $\uparrow$	SSIM $\uparrow$	LPIPS $\downarrow$	Storage $\downarrow$
3DGS <sup>1</sup> [7]	27.71	0.915	0.099	1654.1 MB	30.98	0.922	0.212	368.1 MB	31.73	0.933	0.185	443.6 MB
Mip-Splatting <sup>1</sup> [39]	28.21	<b>0.922</b>	0.096	1108.8 MB	31.49	0.929	0.201	442.8 MB	32.19	0.939	0.177	484.3 MB
Scaffold-GS <sup>1</sup> ( $K = 10$ ) [16]	27.36	0.901	0.122	328.5 MB	30.70	0.927	0.182	840.1 MB	31.20	0.932	0.166	658.5 MB
Scaffold-GS <sup>1</sup> ( $K = 5$ ) [16]	27.32	0.898	0.130	353.7 MB	31.30	0.932	0.170	740.4 MB	31.05	0.930	0.171	593.2 MB
Octree-GS <sup>1</sup> ( $K = 10$ ) [17]	27.07	0.901	0.117	351.0 MB	31.19	0.922	0.212	217.7 MB	32.33	0.939	<b>0.157</b>	372.7 MB
Octree-GS <sup>1</sup> ( $K = 5$ ) [17]	26.93	0.894	0.133	329.9 MB	31.34	0.921	0.224	<b>165.3 MB</b>	31.40	0.929	0.181	403.0 MB
LC-WSR <sup>2</sup> [12]	26.94	0.903	0.111	1670.2 MB	31.84	<b>0.935</b>	<b>0.169</b>	1543.2 MB	32.32	0.937	0.158	1482.7 MB
Ours ( $K = 10$ )	<b>28.80</b>	0.920	<b>0.093</b>	319.2 MB	31.79	0.927	0.218	191.7 MB	32.17	0.934	0.191	<b>176.2 MB</b>
Ours ( $K = 5$ )	28.66	0.914	0.098	<b>262.8 MB</b>	<b>32.27</b>	0.932	0.178	299.0 MB	<b>32.38</b>	<b>0.940</b>	<b>0.157</b>	269.8 MB

<sup>1</sup> Experiments are conducted using the official public repository, with no modifications except for iteration settings as described in Sec. VII-A4.

<sup>2</sup> The official implementation has not been released. Experiments are conducted using our own implementation, which is available at <https://github.com/LiYukeee/sort-free-gs>.

sort are listed to address the effectiveness of our method in reducing the sorting overhead, which is a bottleneck for edge devices.

3) *Baselines*: We compare our method with several SOTA approaches, including 3DGS, Mip-NeRF360, Scaffold-GS, Octree-GS, and LC-WSR. Specifically, LC-WSR serves as the baseline for OIT based Gaussian Splatting rendering, while the remaining methods employ the  $\alpha$ -blending paradigm used in the vanilla 3DGS.

4) *Implementation Details*: For the baseline models, we utilize the sum of the  $\ell_1$  and SSIM losses as the loss function, with the weight  $\lambda_1$  in Eq. 18 is set to 0.2. For comparison, the perceptual loss is computed every 20 training iterations, with  $\lambda_2$  set to 0.5. For neural Gaussian based models (Scaffold-GS, Octree-GS, and the proposed Duplex-GS), experiments are conducted with encoding dimensions  $K$  set to 5 and 10 respectively.

For small-scale scenes containing hundreds of training im-

ages, training is performed for 40,000 iterations, with densification ending after 25,000 iterations. For large-scale scenes containing thousands of training images, training extends to 100,000 iterations, and densification concludes at 50,000 iterations. All experiments are conducted on a single NVIDIA RTX 4090 GPU.

## B. Results Analysis

We first validate our methods by showing that it achieves the highest accuracy across several datasets. The results are shown in Tab. I and Tab. II.

1) *Quantitative Results*: Tab. I presents a comprehensive comparison of our method with several SOTA baselines on three real-world datasets. On the Mip-NeRF dataset, our approach achieves the highest PSNR when  $K = 10$ , outperforming all baselines. While Mip-Splatting and Octree-GS attain slightly higher SSIM values (0.816), our method yields

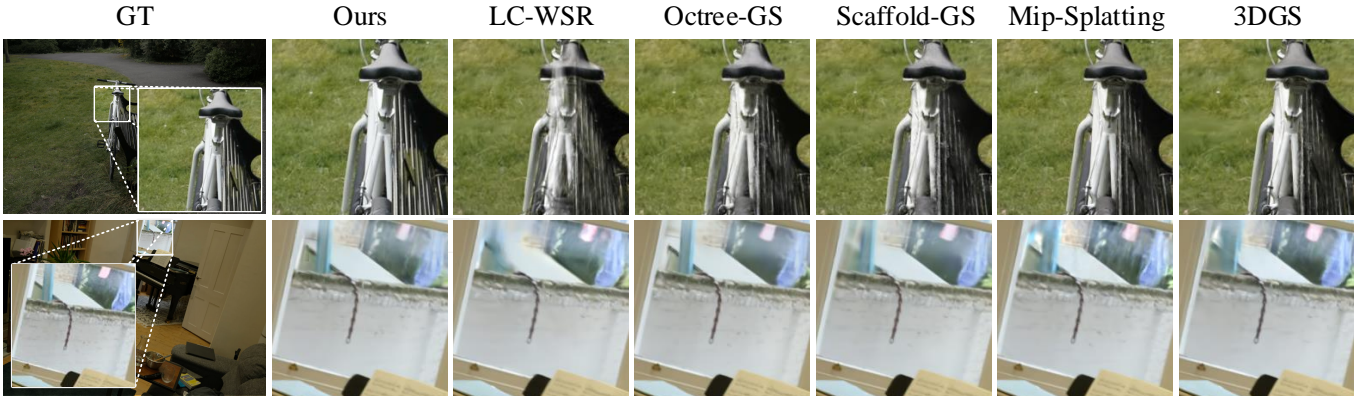


Fig. 6. Qualitative comparisons of Duplex-GS and competing baselines on Mip-NeRF360 [36] dataset. The proposed Duplex-GS successfully removes the “transparency” artifacts for the WSR rendering kernel while maintaining the ability to reconstruct fine details.

competitive SSIM (0.813) and achieves improved perceptual quality, as evidenced by a lower LPIPS (0.216). Remarkably, our model also demonstrates strong storage efficiency, requiring significantly less memory than methods such as 3DGS and Mip-Splatting, both of which demand over 750 MB.

On the Tanks&Temples and Deep Blending datasets, although the PSNR values of our approach are marginally lower, it delivers superior visual quality, attaining the highest SSIM and markedly lower LPIPS compared to other models. Notably, when compared to LC-WSR—the OIT variant of Gaussian Splatting—our method achieves better performance across all metrics and datasets, showing the effectiveness of the OIT paradigm in Gaussian Splatting on CUDA based high-end GPUs.

To further assess our method under challenging scenarios involving multi-scale training views and large-scale datasets—common in real-world applications—we conduct experiments on the BungeeNeRF and VR-NeRF datasets (results shown in Table II). On BungeeNeRF, our approach achieves the highest PSNR and lowest LPIPS when  $K = 10$ , and remains highly competitive with  $K = 5$ , attaining the smallest model size among all baselines. The two scenes within VR-NeRF are large-scale, intricate indoor environments containing thousands of training images. Experimental results indicate that OIT based rendering consistently outperforms sort based  $\alpha$ -blending approaches for such cases, and our proposed method achieves the highest overall accuracy among all evaluated baselines.

2) *Qualitative Results*: We present qualitative results and comparisons with SOTA baselines to demonstrate the effectiveness of our proposed method in artifact removal and detail preservation. As illustrated in Fig. 6 using examples from the Mip-NeRF360 dataset, our method eliminates the “transparency” artifacts observed in the previous OIT based Gaussian model, LC-WSR, while maintaining intricate scene details. For multi-scale and large-scale scenarios, as shown in Fig. 7, the proposed Duplex-GS successfully captures fine details, even in textureless and marginal regions. Additionally, our approach effectively removes “popping” artifacts, benefiting from the OIT blending kernel (see Fig. 8).

TABLE III  
EFFICIENCY ANALYSIS OF DUPLEX-GS AND COMPETING BASELINES.

Method	Mip-NeRF360	Tan.&Tem.	Deep Blend.	BungeeNeRF
3DGS [7]	149	142	145	52
Scaffold-GS [16]	150	129	185	72
Octree-GS [17]	183	159	271	114
LC-WSR [12]	77	89	114	31
Ours	184	147	232	124

3) *Efficiency Analysis*: Tab. III provides a comparison of rendering speeds, measured in FPS, between our method and several state-of-the-art baselines across four benchmark datasets. Our approach consistently achieves the highest or highly competitive FPS on all datasets. On the Mip-NeRF360 dataset, our method achieves 184 FPS, surpassing all other baselines and comparable to the fastest prior approach, Octree-GS (183 FPS). For the Tanks & Temples dataset, our method obtains 147 FPS, demonstrating performance close to the best-performing baseline. While on the Deep Blending dataset, our FPS of 232 is similarly on par with the leading method. Most notably, on the BungeeNeRF dataset, our method achieves 124 FPS, a considerable improvement over existing baselines. These results highlight the efficiency and scalability of our approach, demonstrating real-time rendering capability and practical superiority in intricate and multi-scale scenarios.

Radix sort is employed in 3DGS to determine the explicit ordering of Gaussian primitives, sorting  $b$ -digit numbers with  $m$  possible values in  $\mathcal{O}(b \cdot (n + m))$  time and  $\mathcal{O}(n + m)$  space. Notably, the sequence length  $n$  contributes linearly to the overall complexity. To evaluate the effectiveness of our approach in reducing the computational and memory requirements of view-adaptive sorting, we record the sorting length and corresponding memory consumption during the radix sort procedure. The results, presented in Tab. IV, show that our method successfully mitigates the sorting overhead by introducing cell proxies, thereby demonstrating superior efficiency compared to existing approaches.

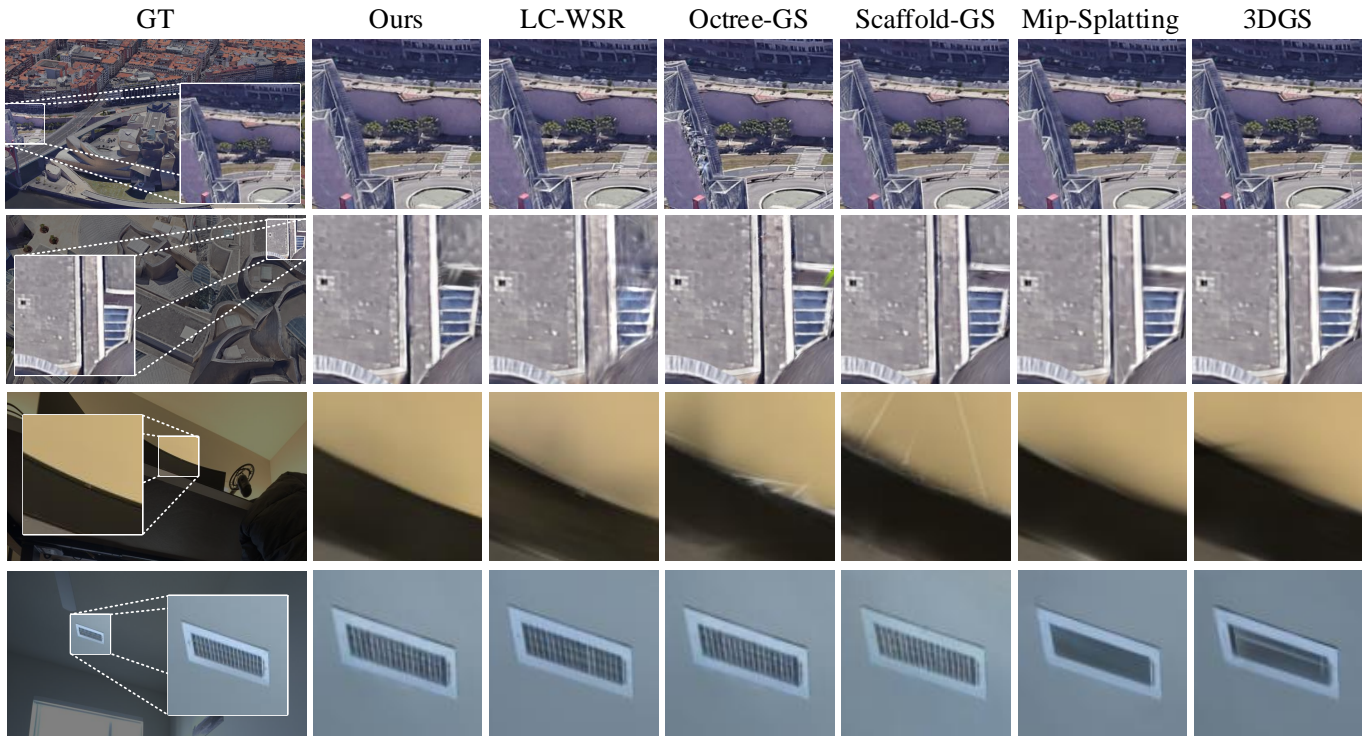


Fig. 7. Qualitative comparisons of Duplex-GS and competing baselines on BungeeNeRF [36] and VR-NeRF [1] datasets. the proposed Duplex-GS successfully captures fine details, even in textureless and marginal regions.

TABLE IV

COMPARISONS ABOUT THE OVERHEAD OF RADIX SORT STAGE. THE PROPOSED CELL RASTERIZATION CONSISTENTLY REDUCE BOTH THE TIME AND SPACE CONSUMPTIONS COMPARED WITH THE VANILLA 3DGS RASTERIZATION.

Method	Mip-NeRF360		BungeeNeRF	
	Sorting Length $\downarrow$	Memory $\downarrow$	Sorting Length $\downarrow$	Memory $\downarrow$
3DGS [7]	7,000,602	81.0 MB	21,798,876	255.0 MB
Ours	3,217,845	37.7 MB	2,843,604	33.3 MB

### C. Ablation Studies

1) *Early Termination*: The introduction of the early termination mechanism is a key advantage of our method over previous approaches such as LC-WSR. To visualize the mechanism, we record the termination ratio with

$$r^{ET} = 1 - \frac{N^{\text{rendered}}}{N^{\text{val}}}, \quad (19)$$

where  $N^{\text{rendered}}$  denotes the number of Gaussians contributed to the final color,  $N^{\text{val}}$  denotes that of the total interacted valid Gaussians along the ray. The results are visualized in Fig. 9. Our method demonstrates termination behavior which closely matches that of the vanilla 3DGS, whereas prior sort-free Gaussian Splatting methods lack this feature. To evaluate its effectiveness, we conduct an ablation study by disabling early termination during model training. As shown in Tab. V, enabling early termination leads to improvements in both accuracy and efficiency.

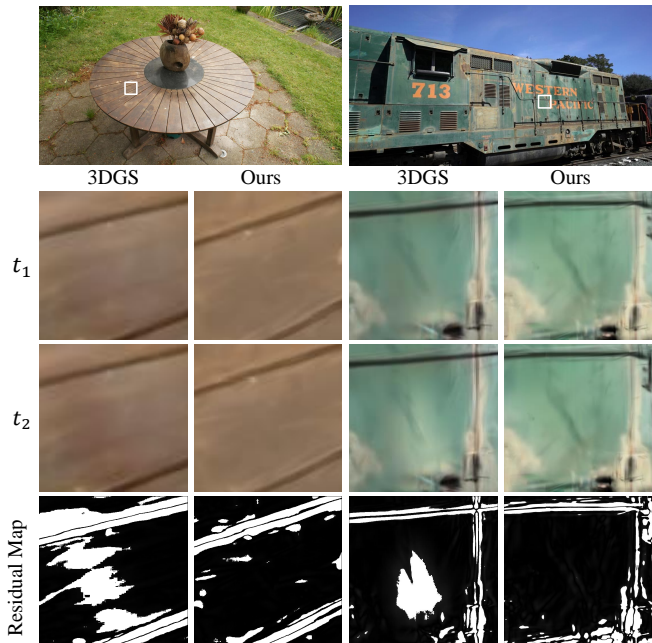


Fig. 8. Illustration of “popping” artifacts removal by recording the differences between contiguous timestep.

2) *Cell Geometry Restriction*: Compared with anchor, cell has specific geometry, restricted by Eq. 12 and Eq. 13, to align the regions between cell and the corresponding Gaussians. To show the effects of these conditions, we mute these restriction and the results are shown in Tab. V. The accuracy decreases as

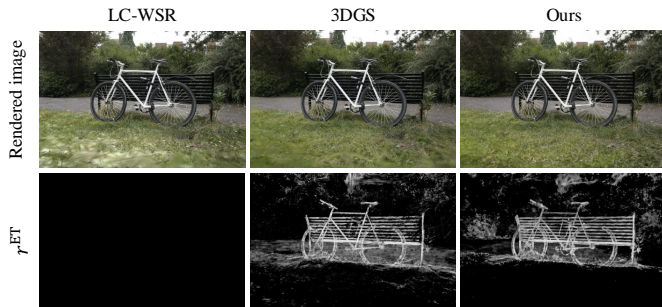


Fig. 9. Visualization of the early termination mechanism. The existing OIT 3DGS method, LC-WSR, does not support early termination due to its sort-free design. In contrast, Duplex-GS achieves termination results comparable to those of vanilla 3DGS, without requiring an explicit Gaussian order.

TABLE V  
ABLATION EXPERIMENTS.

Method	PSNR $\uparrow$	SSIM $\uparrow$	LPIPS $\downarrow$	FPS $\uparrow$
w/o early termination	27.66	0.801	0.220	155
w/o cell restriction	27.54	0.799	0.223	229
w/o $v_i$	27.59	0.801	0.218	174
Full method	27.74	0.802	0.218	184

expected, however, the rendering speed is improved, which is regarded as the compromise between accuracy and efficiency.

3) *Transmittance Design*: As the sorting results of cell level cannot reflect the exact order of Gaussians, we introduce learnable parameter  $v_i$  to compensate the ambiguity. We train models without  $v_i$  to show its effectiveness. The results are shown in Tab. V. By introducing  $v_i$ , the accuracy is improved and the efficiency is slightly improved due to the different amount of cell primitives.

## VIII. LIMITATION AND CONCLUSION

In this work, we propose a dual-layered Gaussian model that effectively resolves the “popping” artifacts present in vanilla 3DGS and the “transparency” artifacts associated with OIT Gaussian Splatting. Leveraging cell search rasterization and an OIT weighted blending technique, our approach substantially reduces the overhead of global sorting. Implemented with CUDA, our method reconstructs intricate scene details while maintaining real-time rendering speed, thereby demonstrating the practicality and effectiveness of the OIT rendering paradigm for Gaussian Splatting models.

Nevertheless, several limitations remain. Specifically, the geometric relationships between cells and Gaussians are not yet fully explored, leading to performance degradation due to intervals as illustrated in Fig. 5. Additionally, while our current implementation is based on CUDA devices, it does not yet exploit intra-cell parallelism for Gaussian blending. Future work will aim to address these limitations, including efficient implementation on specialized hardware such as Field-Programmable Gate Array (FPGA) and Application-Specific Integrated Circuit (ASIC).

## REFERENCES

- [1] L. Xu, V. Agrawal, W. Laney, T. Garcia, A. Bansal, C. Kim, S. Rota Bulò, L. Porzi, P. Kotschieder, A. Božič, D. Lin, M. Zollhöfer, and C. Richardt, “VR-NeRF: High-Fidelity Virtualized Walkable Spaces,” in *Proc. ACM SIGGRAPH Asia*, 2023.
- [2] W. Liu, Y. Zhong, Y. Li, X. Chen, J. Cui, H. Zhang, L. Xu, X. Lou, Y. Shi, J. Yu, and Y. Zhang, “CityGo: Lightweight Urban Modeling and Rendering with Proxy Buildings and Residual Gaussians,” *arXiv preprint arXiv:2505.21041*, 2025.
- [3] W. Li, X. Pan, J. Lin, P. Lu, D. Feng, and W. Shi, “FRPGS: Fast, Robust, and Photorealistic Monocular Dynamic Scene Reconstruction with Deformable 3D Gaussians,” *IEEE Trans. Circuits Syst. Video Technol.*, pp. 1–1, 2025.
- [4] R. Hu, X. Wang, Y. Yan, and C. Zhao, “TGAvatar: Reconstructing 3D Gaussian Avatars with Transformer-based Tri-plane,” *IEEE Trans. Circuits Syst. Video Technol.*, pp. 1–1, 2025.
- [5] Z. Guo, W. Zhou, L. Li, M. Wang, and H. Li, “Motion-Aware 3D Gaussian Splatting for Efficient Dynamic Scene Reconstruction,” *IEEE Trans. Circuits Syst. Video Technol.*, vol. 35, no. 4, pp. 3119–3133, 2025.
- [6] B. Mildenhall, P. P. Srinivasan, M. Tancik, J. T. Barron, R. Ramamoorthi, and R. Ng, “NeRF: Representing Scenes as Neural Radiance Fields for View Synthesis,” in *Proc. Eur. Conf. Comput. Vis. (ECCV)*, 2020.
- [7] B. Kerbl, G. Kopanas, T. Leimkühler, and G. Drettakis, “3D Gaussian Splatting for Real-Time Radiance Field Rendering,” *ACM Trans. Graph.*, vol. 42, no. 4, 2023.
- [8] Y. Bao, T. Ding, J. Huo, Y. Liu, Y. Li, W. Li, Y. Gao, and J. Luo, “3d gaussian splatting: Survey, technologies, challenges, and opportunities,” *IEEE Trans. Circuits Syst. Video Technol.*, pp. 1–1, 2025.
- [9] X. Feng, H. Wang, C. Tang, T. Wu, H. Yang, and Y. Liu, “1.78mJ/Frame 373fps 3D GS Processor Based on Shape-Aware Hybrid Architecture Using Earlier Computation Skipping and Gaussian Cache Scheduler,” in *IEEE Int. Solid-State Circuits Conf. (ISSCC)*, vol. 68, 2025, pp. 1–3.
- [10] S. Song, S. Kim, W. Park, J. Park, S. An, G. Park, M. Kim, and H.-J. Yoo, “IRIS: A 8.55mJ/frame Spatial Computing SoC for Interactive Rendering and Surface-Aware Modeling with 3D Gaussian Splatting,” in *IEEE Int. Solid-State Circuits Conf. (ISSCC)*, vol. 68, 2025, pp. 1–3.
- [11] L. Radl, M. Steiner, M. Parger, A. Weinrauch, B. Kerbl, and M. Steinberger, “StopThePop: Sorted Gaussian Splatting for View-Consistent Real-time Rendering,” *ACM Trans. Graph.*, vol. 43, no. 4, 2024.
- [12] Q. Hou, R. Rauwendaal, Z. Li, H. Le, F. Farhadzadeh, F. Porikli, A. Bourd, and A. Said, “Sort-free gaussian splatting via weighted sum rendering,” in *Proc. Int. Conf. Learn. Represent. (ICLR)*, 2025.
- [13] H. Meshkin, “Sort-Independent Alpha Blending,” *GDC Talk*, vol. 2, no. 4, 2007.
- [14] C. Everitt, “Interactive order-independent transparency,” *White paper, nVIDIA*, vol. 2, no. 6, p. 7, 2001.
- [15] M. McGuire and L. Bavoil, “Weighted Blended Order-Independent Transparency,” *Journal of Computer Graphics Techniques*, vol. 2, no. 4, 2013.
- [16] L. Li, Z. Shen, Z. Wang, L. Shen, and L. Bo, “Scaffold-GS: Structured 3D Gaussians for View-Adaptive Rendering,” in *Proc. IEEE/CVF Conf. Comput. Vis. Pattern Recog. (CVPR)*, 2024, pp. 4222–4231.
- [17] K. Ren, L. Jiang, T. Lu, M. Yu, L. Xu, Z. Ni, and B. Dai, “Octree-GS: Towards Consistent Real-time Rendering with LOD-Structured 3D Gaussians,” *arXiv preprint arXiv:2403.17898*, 2024.
- [18] N. Snavely, S. M. Seitz, and R. Szeliski, “Skeletal Graphs for Efficient Structure from Motion,” in *Proc. IEEE/CVF Conf. Comput. Vis. Pattern Recog. (CVPR)*, 2008, pp. 1–8.
- [19] J. L. Schönberger and J.-M. Frahm, “Structure-from-Motion Revisited,” in *Proc. IEEE/CVF Conf. Comput. Vis. Pattern Recog. (CVPR)*, 2016, pp. 4104–4113.
- [20] Y. Furukawa and J. Ponce, “Accurate, Dense, and Robust Multiview Stereopsis,” *IEEE Trans. Pattern Anal. Mach. Intell.*, vol. 32, no. 8, pp. 1362–1376, 2010.
- [21] Y. Yao, Z. Luo, S. Li, T. Fang, and L. Quan, “MVSNet: Depth Inference for Unstructured Multi-view Stereo,” in *Proc. Eur. Conf. Comput. Vis. (ECCV)*, 2018, pp. 785–801.
- [22] T. Müller, A. Evans, C. Schied, and A. Keller, “Instant Neural Graphics Primitives with a Multiresolution Hash Encoding,” *ACM Trans. Graph.*, vol. 41, no. 4, 2022.
- [23] W. Liu, X. X. Zheng, Y. Li, T. Y. Al-Naffouri, J. Yu, and X. Lou, “CoARF++: Content-Aware Radiance Field Aligning Model Complexity With Scene Intricacy,” *IEEE Trans. Vis. Comput. Graph.*, pp. 1–14, 2025.
- [24] A. Chen, Z. Xu, A. Geiger, J. Yu, and H. Su, “TensorRF: Tensorial Radiance Fields,” in *Proc. Eur. Conf. Comput. Vis. (ECCV)*, 2022, pp. 333–350.

- [25] Z. Chen, T. Funkhouser, P. Hedman, and A. Tagliasacchi, "MobileNeRF: Exploiting the Polygon Rasterization Pipeline for Efficient Neural Field Rendering on Mobile Architectures," in *Proc. IEEE/CVF Conf. Comput. Vis. Pattern Recog. (CVPR)*, 2023, pp. 16569–16578.
- [26] J. Liu, L. Kong, J. Yan, and G. Chen, "Mesh-Aligned 3D Gaussian Splatting for Multi-Resolution Anti-Aliasing Rendering," *IEEE Trans. Circuits Syst. Video Technol.*, pp. 1–1, 2025.
- [27] W. Morgenstern, F. Barthel, A. Hilsman, and P. Eisert, "Compact 3D Scene Representation via Self-Organizing Gaussian Grids," *arXiv preprint arXiv:2312.13299*, 2023.
- [28] S. Niedermayr, J. Stumpfegger, and R. Westermann, "Compressed 3D Gaussian Splatting for Accelerated Novel View Synthesis," in *Proc. IEEE/CVF Conf. Comput. Vis. Pattern Recog. (CVPR)*, 2024, pp. 10349–10358.
- [29] Z. Fan, K. Wang, K. Wen, Z. Zhu, D. Xu, and Z. Wang, "LightGaussian: Unbounded 3D Gaussian Compression with 15x Reduction and 200+ FPS," *arXiv preprint arXiv:2312.13299*, 2023.
- [30] L. Bavoil and K. Myers, "Order Independent Transparency with Dual Depth Peeling," *NVIDIA OpenGL SDK*, vol. 1, no. 12, pp. 2–4, 2008.
- [31] L. Carpenter, "The A-buffer, an Antialiased Hidden Surface Method," in *Proc. ACM SIGGRAPH*, 1984, pp. 103–108.
- [32] M. Salvi and K. Vaidyanathan, "Multi-Layer Alpha Blending," in *Proc. ACM SIGGRAPH Symp. Interact. 3D Graph. Games*, 2014, pp. 151–158.
- [33] Z. Wang, A. Bovik, H. Sheikh, and E. Simoncelli, "Image Quality Assessment: From Error Visibility to Structural Similarity," *IEEE Trans. Image Process.*, vol. 13, no. 4, pp. 600–612, 2004.
- [34] C. Ledig, L. Theis, F. Huszar, J. Caballero, A. Cunningham, A. Acosta, A. Aitken, A. Tejani, J. Totz, Z. Wang, and W. Shi, "Photo-Realistic Single Image Super-Resolution Using a Generative Adversarial Network," in *Proc. IEEE/CVF Conf. Comput. Vis. Pattern Recog. (CVPR)*, 2017.
- [35] X. Wang, K. Yu, S. Wu, J. Gu, Y. Liu, C. Dong, C. C. Loy, Y. Qiao, and X. Tang, "ESRGAN: Enhanced Super-Resolution Generative Adversarial Networks," in *Proc. Eur. Conf. Comput. Vis. (ECCV)*, 2018.
- [36] J. T. Barron, B. Mildenhall, D. Verbin, P. P. Srinivasan, and P. Hedman, "Mip-NeRF 360: Unbounded Anti-Aliased Neural Radiance Fields," in *Proc. IEEE/CVF Conf. Comput. Vis. Pattern Recog. (CVPR)*, 2022, pp. 5855–5864.
- [37] A. Knapitsch, J. Park, Q.-Y. Zhou, and V. Koltun, "Tanks and Temples: Benchmarking Large-Scale Scene Reconstruction," *ACM Trans. Graph.*, vol. 36, no. 4, 2017.
- [38] P. Hedman, J. Philip, T. Price, J.-M. Frahm, G. Drettakis, and G. Brostow, "Deep Blending for Free-Viewpoint Image-Based Rendering," *ACM Trans. Graph.*, vol. 37, no. 6, 2018.
- [39] Z. Yu, A. Chen, B. Huang, T. Sattler, and A. Geiger, "Mip-Splatting: Alias-free 3D Gaussian Splatting," in *Proc. IEEE/CVF Conf. Comput. Vis. Pattern Recog. (CVPR)*, June 2024, pp. 19447–19456.
- [40] Y. Xiangli, L. Xu, X. Pan, N. Zhao, A. Rao, C. Theobalt, B. Dai, and D. Lin, "BungeeNeRF: Progressive Neural Radiance Field for Extreme Multi-scale Scene Rendering," in *Proc. Eur. Conf. Comput. Vis. (ECCV)*, 2022.
- [41] R. Zhang, P. Isola, A. A. Efros, E. Shechtman, and O. Wang, "The Unreasonable Effectiveness of Deep Features as a Perceptual Metric," in *Proc. IEEE/CVF Conf. Comput. Vis. Pattern Recog. (CVPR)*, 2018.



**Yuke Li** received the B.S. degree in data science from China University of Petroleum, Qingdao, China, in 2024. He is currently pursuing the master's degree with ShanghaiTech University, Shanghai, China. His research interests include AI, neural networks, and data science.



**Yuxuan Li** Yuxuan Li received the B.S. degree in microelectronics science and engineering from Shanghai University in 2025. He is currently pursuing the doctoral degree at ShanghaiTech University. His research interests include computer graphics and computer architecture.



**Jingyi Yu** (Fellow, IEEE) received the B.S. degree from Caltech in 2000 and the Ph.D. degree from MIT in 2005. He is currently the Vice Provost with ShanghaiTech University. Before joining ShanghaiTech University, he was a Full Professor with the Department of Computer and Information Sciences, University of Delaware. His current research interests include computer vision and computer graphics, especially computational photography and nonconventional optics and camera designs. He is a recipient of the NSF CAREER Award and the AFOSR

YIP Award. He served as an Area Chair for many international conferences, including CVPR, ICCV, ECCV, IJCAI, and NeurIPS. He was the Program Chair of CVPR 2021 and will be the Program Chair of ICCV 2025.



**Xin Lou** (Senior Member, IEEE) received the B.Eng. degree in Electronic Information Technology and Instrumentation from Zhejiang University (ZJU), China, in 2010 and M.Sc. degree in System-on-Chip Design from Royal Institute of Technology (KTH), Sweden, in 2012 and PhD degree in Electrical and Electronic Engineering from Nanyang Technological University (NTU), Singapore, in 2016. Then he joined VIRTUS, IC Design Centre of Excellence at NTU as a research scientist. He is currently an Associate Professor with the School of Information Science and Technology, ShanghaiTech University, Shanghai, China. His research interests primarily focus on high-performance and energy-efficient integrated circuits and systems for vision and graphics processing. Dr. Lou serves as an Associate Editor of IEEE Transactions on Very Large Scale Integration, and was an Associate Editor of IEEE Transactions on Circuits and Systems II: Express Briefs (2022-2023), a Guest Editor of Associate Editor of IEEE Transactions on Circuits and Systems I (2024).



**Weihang Liu** received the B.S. and M.E. degree in electronics and communication engineering in 2019 and 2022. He is currently working toward the doctoral degree in electronic and information engineering with School of Information Science and Technology, ShanghaiTech University, Shanghai, China. His research interests include computer graphics, computer vision and artificial intelligence.